Synthesis and Optical Properties of ZnO Nanostructures

Li Li Yang

Linköping University

INSTITUTE OF TECHNOLOGY

Physical Electronic Division

Department of Science and Technology

Linköping University, SE-601 74 Norrköping, Sweden

Synthesis and optical properties of ZnO nanostructures

LILI YANG

Department of Science and Technology (ITN), Campus Norrköping, Linköping University, SE-601 74 Norrköping, Sweden

Abstract

One-dimensional ZnO nanostructures have great potential applications in the fields of optoelectronic and sensor devices. Therefore, it is really important to realize the controllable growth of one-dimensional ZnO nanostructures and investigate their properties. The main points for this thesis are not only to successfully realize the controllable growth of ZnO nonawires, nanorods and quantum dots (QDs), and also investigate the structure and optical properties in detail by the methods of scan electron microscope(SEM), transmission electron microscope(TEM), resonant Raman, photoluminescence(PL) and low-temperature time resolved PL spectrum.

In this thesis, on one hand, the two-step chemical bath deposition method was used to grown ZnO nanorod arrays (ZNAs) on Si substrates. Firstly, the effects of ZnO nanoparticles, pH value of chemical solution, angel θ between substrate and beaker bottom on the structures of the samples were symmetrically investigated and the optimized growth condition to grow ZNAs can be concluded as follows: seed layer of ZnO nanoparticles, pH=6 and θ=70˚. On the basis of these, the diameter of ZNAs was well controlled from 150nm~40nm through adjusting the diameter and density of the ZnO nanoparticles pretreated on the Si substrates. The experimental results indicated that both diameter and density of ZnO nanoparticles on the substrates determined the diameter of ZNAs. But when the density is higher than the critical value of $2.3 \times 10^8 \mathrm{cm}^{-2}$, the density will become the dominant factor to determine the diameter of ZNAs.

One the other hand, the optical properties of ZNAs were investigated in detail. The Raman and photoluminescence (PL) results showed that after an annealing treatment around $500^{\circ}\mathrm{C}$ in air atmosphere, the crystal structure and optical properties became much better due to the decrease of surface defects. The resonant Raman measurements excited by 351.1nm not only revealed that the surface defects play a significant role in the as-grown sample, but also suggested that the strong intensity increase of some Raman scatterings was due to both outgoing resonant Raman scattering effect and deep level defects scattering contribution for ZnO nanorods annealed from 500°C to 700°C. It is the first time to the best of our knowledge that the Raman measurements can be used to monitor the change of surface defects and deep level defects in the CBD grown ZnO nanorods. We have also presented, for the first time, a time resolved PL study in CBD grown ZnO nanorods with different diameters. The results show that the decay time of the excitons in the nanorods strongly depends on the diameter of the nanorods. The altered decay time is mainly due to the surface recombination process. The effective time constant related to the surface recombination velocity was deduced. A thermal treatment under 500°C will suppress the surface recombination channel, resulting in an improvement of the optical quality for the ZnO nanorods.

This thesis not only provides the effective way to control the size of ZNAs, but also obtains some beneficial results in aspects of their optical properties, which builds theoretical and experimental foundation for much better and broader applications of one-dimensional ZnO nanostructures.

Keywords: ZnO nanorods; size-controllable growth; post-annealing; optical properties

List of publications

This thesis contains an introductory text and the following papers:

Paper I

Size-controlled growth of well-aligned ZnO nanorod arrays with two-step chemical bath deposition method
L.L. Yang, Q.X. Zhao and Magnus Willander
Journal of Alloys and Compounds, in press (2008)

Paper II

Effective way to control the size of well-aligned ZnO nanorod arrays with two-step chemical bath deposition
L.L. Yang, Q.X. Zhao, M. Willander, J.H.Yang
Submitted

Paper III

Effects of annealing on optical properties of low temperature grown ZnO nanorod arrays
L.L. Yang, Q.X. Zhao, M. Willander, J.H.Yang, I. Ivanov and E. Zanghellini
Submitted

Paper IV

Surface Recombination in ZnO Nanorods Grown by Chemical Bath Deposition
Q.X. Zhao, L.L. Yang, M. Willander, B. E. Sernelius and P.O. Holtz
Journal of Applied Physics, in press (2008)

Additional papers not included in this thesis

M. Riaz, A. Ful, **L. L. Yang**, O. Nur, M. Willander, and P. Klason
Bending flexibility, kinking and buckling characterization of ZnO nanorods/nanowires grown on different substrates by high and low temperature methods
Journal of Applied Physics, in press (2008)

M. Willander, **L. L. Yang,** A. Wadeasa, S. U. Ali, M. H. Asif, Q. X. Zhao, and O. Nur
Zinc oxide nanowires: controlled low temperature growth and some electrochemical and optical devices
Journal of Materials Chemistry, in press (2008)

M. Willander, P. Klason, **L. L. Yang**, Safaa M. Al-Hilli, Q. X. Zhao, O. Nur
ZnO nanowires: chemical growth, electrodeposition, and application to intracellular nano-sensors
Physica Status Solidi C 2008, vol. 5, no. 9, pp. 3076-3083

M. Willander, A.Wadeasa, P. Klason, **L.L. Yang**, S. Lubana Beegum, S. Raja, Q.X. Zhao, O. Nur
Light-emitting diodes based on n-ZnO nano-wires and p-type organic semiconductors
Proceedings of the SPIE - The International Society for Optical Engineering, v 6895, 7 Feb. 2008, p 68950O-1-10

Q.X. Zhao, **L.L. Yang**, M. Willander, G. Pozina and P.O. Holtz
Surface Recombination in ZnO Nanorods Grown by Aqueous Chemical Method
29th The International Conference on the Physics of Semiconductors, 27/7-1/8 2008 in Rio De Janero, Brazil

M. Willander, A. Wadeasa, **Lili Yang**, Q.X.Zhao, and O. Nur
Light emitting didoes based on n-ZnO nanowires and p-type organic semiconductors
Photonic West, Integrated Optoelectronic Devices Symposium, San Jose California, January (2008)

L.L. Yang, Q.X. Zhao and M. Willander
In Book, Quantum Wells: Theory, Fabrication and Applications, by Nova Science Publishers, Inc. (2008), One Chapter "Coupled Quantum Well Structures",

Acknowledgements

At the time when I just finished the entire thesis, I am sitting in front of the computer and looking back the whole one and a half years in Linköping University, I can not find exact words to express how I appreciate and cherish this wonderful life.

First of all, I would like to express my appreciation to my main supervisor Associate Prof. Qingxiang Zhao, co-supervisor Prof. Magnus Willander and leader Prof. Jinghai Yang in China who provides this huge opportunity for me and brings me into this warm family, our physics electronic Willander group. Therefore, I have a chance to have a brilliant new life in Sweden which I will never forget for my whole life.

I would like to express my gratitude to my main supervisor Qingxiang Zhao again for your patient guide and tutor in the whole research work and kind help for my daily life in Sweden. Without your support and input this thesis would not have been completed so fast. Particularly, you help me open a new door when I only have a small window to look into the physics world. It is my honor to be your student and I am really proud of it.

I would also like to thank my co-supervisor Prof. Magnus Willander again for your guide, help, encouragement, support and trust all the times. You keep working so hard to create the great research environment for our group and so kind to do your best to support your students for their future. What you do will always remind me how to become a good teacher and even a great group leader if I have that chance in my future.

I would also like to thank Associate Prof. Omer Nour and our group's research coordinator Lise-Lotte Lönndahl Ragnar for their kind and patient helps for my work and life.

Amal, Alim, Riaz, Isra, and all the other group members. Thank you for all your friendship and help. Amal, you just like my sister, thank you for sharing all my sad and happy moments, and also for always encouragement, support and help. I can feel the warm even in the cold winter because of you.

For my parents and younger sister, words are not enough to express my gratitude for you. Without your selfless love and endless support, I can not be me today. Thank you for always being there!

At last but not at least, my dear husband Helei Lu, deeply thanks for love, support and everything you have done for me.

Lili Yang
Norrköping 2008-10-19

Contents

Chapter 1

Introduction

Nowadays, the products of semiconductor industry spread all over the world and deeply penetrate into the daily life of human being. The starting point of semiconductor industry was the invention of the first semiconductor transistor at Bell Lab in 1947. Since then, the semiconductor industry has kept growing enormously. In the 1970's, the information age of human being was started on the basis of the stepwise appearance of quartz optical fiber, III-V compound semiconductors and gallium arsenide (GaAs) lasers. During the development of the information age, silicon (Si) keeps the dominant place on the commercial market, which is used to fabricate the discrete devices and integrated circuits for computing, data storage and communication. Since Si has an indirect band gap which is not suitable for optoelectronic devices such as light emitting diodes (LED) and laser diodes, GaAs with direct band gap stands out and fills the blank for this application. As the development of information technologies, the requirement of ultraviolet (UV)/blue light emitter applications became stronger and stronger which is beyond the limits of GaAs. Therefore, the wide bandgap semiconductors such as SiC, GaN and ZnO, i.e. the third generation semiconductors, come forth and turn into the research focus in the field of semiconductor.

The research interest in ZnO, one of wide band gap semiconductors, has waxed and waned over the years. The first enthusiasm started studies of the lattice parameter by M.L. Fuller in 1929 [1] and C.W.Bunn's study in 1935[2], but the enthusiasm flagged with the difficulty in producing p-type doping and high quality crystal crystalline material. During the last decade the ZnO related research has once more increased rapidly. The number of articles published on ZnO has increased every year and in 2007 ZnO became the second most popular semiconductor materials after Si. On one hand, the popularity to a large extent is due to the improvements in growth of high quality, single crystalline ZnO in both epitaxial layers and bulk form. On the other hand, especially since the emergence of the nanotechnology, novel electrical, mechanical, chemical and optical properties are introduced with the reduction in size, which are largely believed to be the result of surface and quantum confinement effects. Study of one dimensional (1D) materials has become a leading edge in nanoscience and nanotechnology. ZnO is a versatile functional material. 1D ZnO nanostructures such as nanotubes[3], nanowires[4], nanorods[5], nanobelts[6], nanocables[7], and nanoribbons[8] stimulate considerable interests for scientific research due to their importance in fundamental physics studies and their potential applications in nanoelectronics, nanomechanics, and flat panel displays. Particularly, the optoelectronic device application of 1D ZnO nanostructure becomes one of the major focuses in recent nanoscience researches [9-11].

During the last decade, ZnO epilayer, ZnO nanorods and various ZnO nanostructures have been grown by various techniques. A major advantage for ZnO nanostructures, e.g. nanowires and nanorods, is that they can be easily grown on various substrates and non-lattice materials including flexible polymers. In addition, ZnO nanorods can be advantageous with a low density of defects. The growth of

defect-free structures is more likely for nanorods in comparison with epilayers, since the strain in the nanorods can be efficiently relieved by elastic relaxation at the free lateral surfaces rather than by plastic relaxation.

In order to utilize the applications of nanostructure materials, it usually requires that the crystalline morphology, orientation and surface architecture of nanostructures can be well controlled during the preparation processes. As concerned as ZnO nanostructures, although different fabrication methods, such as vapor-phase transport [12-14], pulsed laser deposition [15], chemical vapor deposition [17,17] and electrochemical deposition [18], have been widely used to prepare ZnO nanostructures, the complex processes, sophisticated equipment and high temperatures make them very hard to large-scale produce for commercial application. On the contrary, aqueous chemical method shows its great advantages due to much easier operation and very low temperature (95°C) [19, 20], in addition to low cost. However, the ZnO nanostructures grown by this method show a poor reproducibility, difficulty to control size and bad orientation, particularly on substrates (such as Si) with large lattice mismatch and different crystalline structures in comparison with ZnO. Hence, it is still a significant challenge to obtain controllable growth of ZnO nanostructures.

In terms of application of ZnO nanostructures, it requires not only that their crystalline morphology, orientation and surface architecture be well controlled during the preparation processes, but also an improved quality of their optical and electronic properties. Unfortunately, ZnO nanostructures grown at relatively low temperature usually showed poor crystallization and optical properties. In addition, one of the significant differences between ZnO nanostructures and an epilayer is the larger surface area of the former. This large surface area can be an advantage for some applications, for example sensor devices. However, it can also be a problem in other applications, for example, optoelectronic devices such as light emitting diodes and solar-cell devices, since the surface recombination rate may become dominating, resulting in a short carrier life time. So far, the knowledge about surface recombination in ZnO nanostructures is limited.

Above, the background and the problems for ZnO nanostructures were briefly reviewed. This thesis will be only focused on ZnO nanorods arrays (ZNAs) and expanded on two topics. One topic is how to realize the size controllable growth of ZNAs with chemical bath deposition (CBD) method; the other is the investigation of the surface recombination of ZNAs and how to suppress it in order to improve the optical properties. The first four chapters in the thesis give a brief review of ZnO properties and our experimental details. In Chapter 2, the basic properties of ZnO are introduced. Chapter 3 describes the experimental details used for this work. Finally, the thesis ends with some concluding remarks and outlooks for the future in Chapter 4.

Chapter 2

Structural and Optical Properties of ZnO

ZnO is a key technological material. ZnO is a wide band-gap (3.37 eV) compound semiconductor that is suitable for short wavelength optoelectronic applications. The high exciton binding energy (60meV) in ZnO crystal can ensure efficient excitonic emission at room temperature and room temperature ultraviolet (UV) luminescence has been reported in disordered nanoparticles and thin films. In addition, the lack of a centre of symmetry in wurtzite, combined with large electromechanical coupling, results in strong piezoelectric and pyroelectric properties and the consequent use of ZnO in mechanical actuators and piezoelectric sensors. Furthermore, ZnO is a versatile functional material that has a diverse group of growth morphologies, such as nanocombs, nanorings, nanohelixes/nanosprings,nanobelts, nanowires and nanocages. These ZnO nanostructures are easily formed even on cheap substrates such as glass and hence they have a promising potential in the nanotechnology future. Finally, ZnO nanostructures are also attractive for biomedical application since it is a bio-safe material and its nanostructure has a large surface area. As well as we know, all these applications definitely originate from its basic properties. Therefore, in order to in-depth know about ZnO, the structural and optical properties of ZnO will be introduced in detail in this chapter.

2.1 Crystal and surface structure of ZnO [21]

At ambient pressure and temperature, ZnO crystallizes in the wurtzite (B4 type) structure, as shown in figure 2.1. This is a hexagonal lattice, belonging to the space group P6$_3$*mc* with lattice parameters a = 0.3296 and c = 0.52065 nm. The structure of ZnO can be simply described as a number of alternating planes composed of tetrahedrally coordinated O^{2-} and Zn^{2+} ions, stacked alternately along the c-axis (Figure2.1). The tetrahedral coordination in ZnO results in noncentral symmetric structure and consequently piezoelectricity and pyroelectricity. Another important characteristic of ZnO is polar surfaces. The most common polar surface is the basal plane. The oppositely charged ions produce positively charged Zn-(0001) and negatively charged O-(000$\bar{1}$) surfaces, resulting in a normal dipolemoment and spontaneous polarization along the c-axis as well as a divergence in surface energy. To maintain a stable structure, the polar surfaces generally have facets or exhibit massive surface reconstructions, but ZnO-± (0001) are exceptions: they are atomically flat, stable and without reconstruction [22, 23]. Efforts to understand the superior stability of the ZnO ± (0001) polar surfaces are at the forefront of research in today's surface physics [24–27]. The other two most commonly observed facets for ZnO are {2$\bar{1}$$\bar{1}$0} and {01$\bar{1}$0}, which are non-polar surfaces and have lower energy than the {0001} facets.
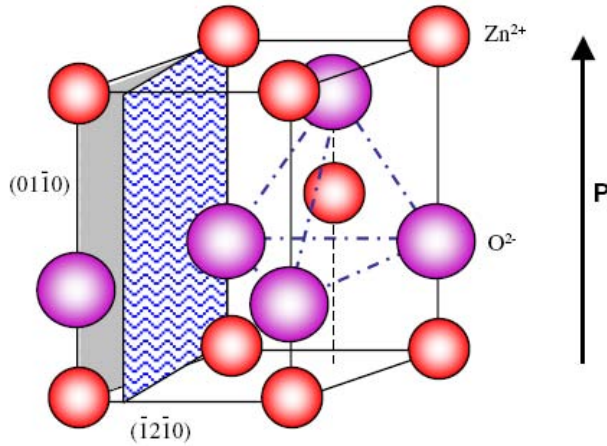
Figure 2.1: The wurtzite structure model of ZnO. The tetrahedral coordination of Zn–O is shown.

Additional to the wurtzite phase, ZnO is also known to crystallize in the cubic zincblende and rocksalt (NaCl) structures, which are illustrated in figure 2.2[28]. Zincblende ZnO is stable only by growth on cubic structures [29–31], while the rocksalt structure is a high-pressure metastable phase forming at ~10 GPa, and can not be epitaxially stabilized [32]. Theoretical calculations indicate that a fourth phase, cubic cesium chloride, may be possible at extremely high temperatures, however, this phase has yet to be experimentally observed [33].
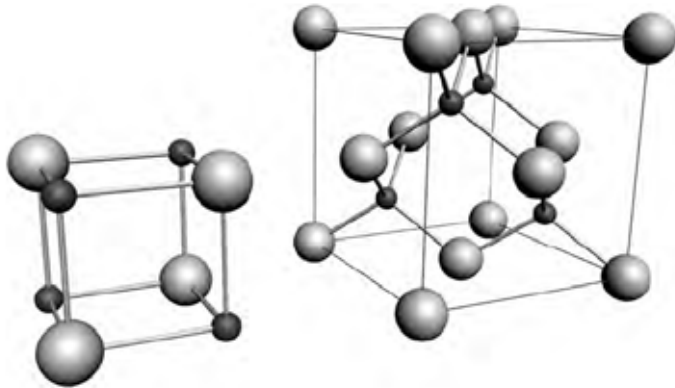

Figure 2.2: The rock salt (left) and zincblende (right) phases of ZnO. O atoms are shown as white spheres, Zn atoms as black spheres. Only one unit cell is illustrated for clarity.

2.2 Basic physical parameters for ZnO

Table 2.1 shows a compilation of basic physical parameters for ZnO [34, 35]. It should be noted that there still exists uncertainty in some of these values. For example, there have few reports of p-type ZnO and therefore the hole mobility and effective mass are still in debate. Similarly, the values for thermal conductivity show some spread in values and this may be a result of the influence of defects such as dislocations [36], as was the case for GaN. The values for carrier mobility will undoubtedly increase as more control is gained over compensation and defects in the material.

Table 2.1: Physical parameters of ZnO

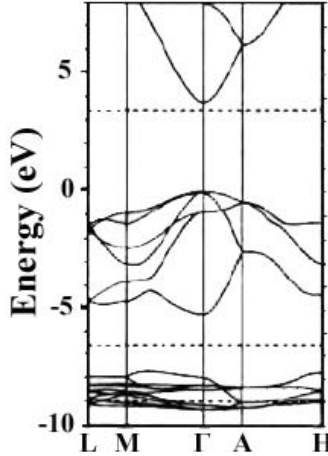| Physical parameters	Values
Lattice parameters at 300 K	
a_0	0.32495 nm
c_0	0.52069 nm
a_0/c_0	1.602 (ideal hexagonal structure shows 1.633)
u	0.345
Density	5.606 g/cm^3
Stable phase at 300 K	Wurtzite
Melting point	1975°C
Thermal conductivity	0.6, 1–1.2
Linear expansion coefficient(/^{o}C)	a_0: 6.5 $\times 10^{-6}$ c_0: 3.0 $\times 10^{-6}$
Static dielectric constant	8.656
Refractive index	2.008, 2.029
Energy gap	3.37 eV, direct
Intrinsic carrier concentration	$<10^6$ cm^{-3} (max n-type doping$>10^{20}$ cm^{-3} electrons; max p-type doping$<10^{17}$ cm^{-3} holes)
Exciton binding energy	60 meV
Electron effective mass	0.24
Electron Hall mobility at 300 K for low n-type conductivity	200 cm^2/V s
Hole effective mass	0.59
Hole Hall mobility at 300 K for low p-type conductivity	5–50 cm^2/V s

2.3 Energy band gap

Figure 2.3: The LDA band structure of bulk wurtzite ZnO calculated using dominant atomic self-interaction-corrected pseudopotentials (SIC-PP). This method is much more efficient at treating the *d*-bands than the standard LDA method. [37]

The electronic band structure of ZnO has been calculated by a number of groups [38–43]. The results of a band structure calculation using the Local Density Approximation (LDA) and incorporating atomic self-interaction corrected pseudopotentials (SIC-PP) to accurately account for the Zn 3*d* electrons is shown in figure 2.3 [43]. The band structure is shown along high symmetry lines in the hexagonal Brillouin zone. Both the valence band maxima and the lowest conduction band minima occur at the Γ point k=0 indicating that ZnO is a direct band gap semiconductor. The bottom 10 bands (occurring around −9 eV) correspond to Zn 3*d* levels. The next 6 bands from −5 eV to 0 eV correspond to O 2*p* bonding states. The first two conduction band states are strongly Zn localized and correspond to empty Zn 3*s* levels. The higher conduction bands (not illustrated here) are free-electron-like. The O2*s* bands (also not illustrated here) associated with core-like energy states, occur around −20 eV. The band gap as determined from this calculation is 3.77 eV. This correlates reasonably well with the experimental value of 3.4 eV, and is much closer than the value obtained from standard LDA calculations, which tend to underestimate the band gap by ~3 eV due to its failure in accurately modeling the Zn 3*d* electrons.

Experimentally, the ZnO valence band is split by crystal field and spin orbit interaction into three states named A, B and C under the wurtzite symmetry. This splitting is schematically illustrated in Figure 2.4. The A and C subbands are known to posses Γ_7 symmetry, whilst the middle band, B, has Γ_9 symmetry [44]. The band gap has the temperature dependence up to 300K given by the relationship:

$$E_g(T) = E_g(T=0)\frac{5.05 \times 10^{-4}T^2}{900-T} \tag{1.1}$$

These properties of ZnO give rise to interesting optical properties which will be discussed in following part.
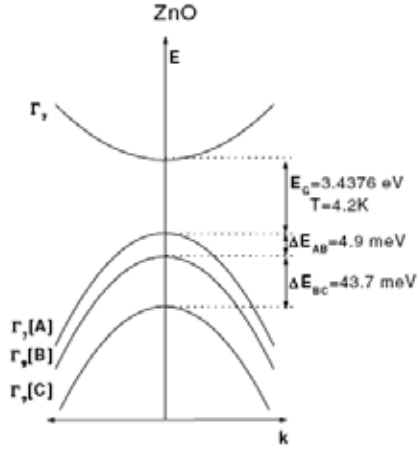
Figure 2.4: Band structure and symmetries of hexagonal ZnO. The splitting into three valence bands (A, B, C) is caused by crystal field and spin-orbit splitting.

2.4 Optical Properties of ZnO

Optical properties and processes in ZnO as well as its refractive index were extensively studied many decades ago. The renewed interest in ZnO is fuelled and fanned by its prospects in optoelectronics applications owing to its direct wide band gap of 3.37 eV at room temperature with large exciton energy of 60 meV and efficient radiative recombination. The strong exciton binding energy, which is much larger than that of GaN (25 meV), and the thermal energy at room temperature (25 meV) can ensure an efficient exciton emission at room temperature under low excitation energy. As a consequence, ZnO is recognized as a promising photonic material in the blue-UV region.

In this section, a review on the optical properties of a semiconductor is given first. The UV emission and origins of deep level emission band (DLE) in ZnO photoluminescence (PL) spectra are briefly discussed next. Finally, the surface recombination is introduced.

2.4.1 Optical properties of semiconductor

The optical properties of a semiconductor have their genesis in both intrinsic and extrinsic effects. Intrinsic optical transitions take place between the electrons in the conduction band and holes in the valence band, including excitonic effects due to the Coulomb interaction. Excitons are classified into free and bound excitons. In high-quality samples with low impurity concentrations, the free excitons can also exhibit excited states, in addition to their ground-state transitions. Extrinsic properties are related to dopants/impurities or point defects and complexes, which usually create electronic states in the bandgap, and therefore influence both optical absorption and emission processes. The electronic states of the bound excitons, which may be bound

7

to neutral or charged donors and acceptors, depend strongly on the semiconductor material, in particular the band structure. For a shallow neutral donor bound exciton, for example, the two electrons in the bound exciton state are assumed to pair off into a two-electron state with zero spin. The additional hole is then weakly bound in the net hole-attractive Coulomb potential set up by this bound two-electron aggregate. Similarly, neutral shallow acceptor bound excitons are expected to have a two-hole state derived from the topmost valence band and one electron interaction. Other extrinsic transitions could be seen in optical spectra such as free-to-bound (electron-acceptor) and bound-to-bound (donor-acceptor).

2.4.2 Optical properties of ZnO

Optical transitions in ZnO have been studied by a variety of experimental techniques such as optical absorption, transmission, reflection, photoreflection, spectroscopic ellipsometry, photoluminescence, cathodoluminescence, calorimetric spectroscopy, etc. It is well known that at room temperature the PL spectrum from ZnO typically consists of a UV emission band and a broad emission band, as shown in Figure 2.5. The UV emission band is dominated by the free exciton (FE) emission. The broad emission band literally between 420 and 700nm observed nearly in all samples regardless of growth conditions is called deep level emission band (DLE). The UV emission band is related to a near band-edge transition of ZnO, namely, the recombination of the free excitons. The deep level emission band has previously been attributed to several defects in the crystal structure such as O-vacancy (V_O) [45-47], Zn-vacancy (V_{Zn})[48-50], O-interstitial (O_i) [51], Zn-interstitial (Zn_i) [52], and extrinsic impurities such as substitutional Cu [53]. Recently, this deep level emission band had been identified and at least two different defect origins (V_O and V_{Zn}) with different optical characteristics were claimed to contribute to this deep level emission band [54-56].
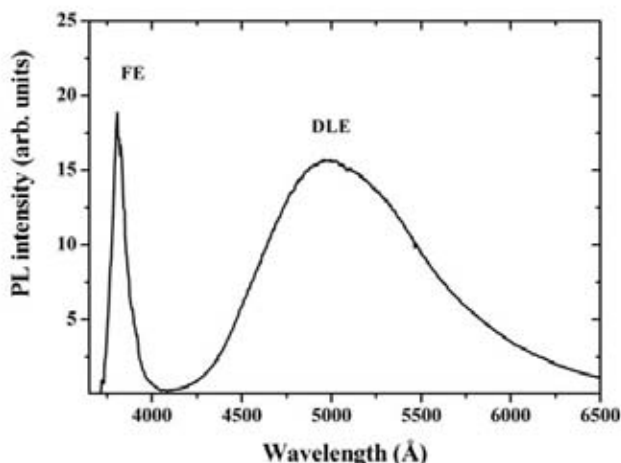
Figure 2.5: PL spectrum of ZnO nanorods from the sample grown on a 1.7 nm thick Au-layer deposited (001) Si substrate at 890 ^{o}C, measured at room temperature with excitation power of 5 mW, the excitation wavelength is 350 nm.
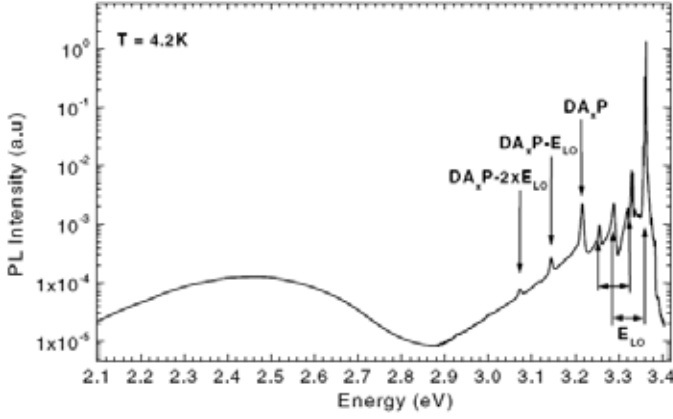
Figure 2.6: Photoluminescence spectrum of bulk ZnO showing excitonic, donor acceptor pair (DAP) and deep level emission. The corresponding phonon replicas with longitudinal optical phonons (LO) are indicated (He-Cd excitation).

Table 2.2: Free and bound exciton recombinations and related properties.

line	wavelength (nm)	energy (eV)	localisation energy (meV)	two-electron-satellite separation $(2P_{xy} - 1S)$ (meV)	donor binding energy (meV)	chemical identity
$A_L{}^*$	367.12	3.3772				
$A_T{}^*$	367.26	3.3759				
I_0	367.63	3.3725	3.4			
I_1	367.71	3.3718	4.1			
I_{1a}	368.13	3.3679	8.0			
$I_2{}^{**}$	368.19	3.3674	8.5			
$I_3{}^{**}$	368.29	3.3665	9.4			
I_{3a}	368.34	3.3660	9.9			
I_4	368.34	3.3628	13.1	34.1	46.1	H
I_5	368.86	3.3614	14.5			
I_6	368.92	3.3608	15.1	38.8	51.55	Al
I_{6a}	368.96	3.3604	15.5	40.4	53	
I_7	369.01	3.3600	15.9			
I_8	369.03	3.3598	16.1	42.1	54.6	Ga
I_{8a}	369.08	3.3593	16.6			
I_9	369.37	3.3567	19.2	50.6	63.2	In
I_{10}	369.76	3.3531	22.8	60.2	72.6	
I_{11}	370.28	3.3484	27.5			

* A_L and A_T are the longitudinal and transversal free A-exciton states. A_T is the reference for the determination of the bound exciton localisation energy.

** I_2 and I_3 are assigned to ionised donor bound exciton recombinations.

At low cryogenic temperatures bound exciton emission is the dominant radiative channel. Figure 2.6 shows a typical photoluminescence spectrum of *n*-type bulk ZnO measured at 4.2 K [57]. The luminescence spectrum from ZnO extends from the band edge to the green/orange spectral range. Very common is a broad band centered about 2.45 eV extending from the blue into the green range. The lines dominating the spectrum originate from bound exciton (BE) recombinations (excitons bound to neutral donors (D_0X) and/or acceptors (A_0X)) followed by longitudinal optical (LO) phonon replicas with an energy separation of 72 meV. The free exciton emission with the A-valence band (FXA) positioned at 3.375 eV can already be seen. And a donor-acceptor-pair (DAP) transition around 3.22 eV is found, which is again followed by phonon replicas.

Until now, up to eleven excitonic recombinations where excitons bind to neutral donors and/or acceptors have been observed [58-62]. The positions of these eleven prominent PL lines are listed in Table 2.2. However, the chemical nature of the donor and acceptor species still remains unclear.

2.4.3 Surface recombination [63]

There are two basic recombination mechanisms in semiconductors, namely *radiative* recombination and *non-radiative* recombination. In a radiative recombination event, one photon with energy equal to or near the bandgap energy of the semiconductor is emitted, as illustrated in Figure 2.7. During non-radiative recombination, the electron energy is converted to vibrational energy of lattice atoms, i.e. phonons. Thus, the electron energy is converted to heat. For obvious reasons, non-radiative recombination events are unwanted in light-emitting devices.

There are mainly three physical mechanisms by which non-radiative recombination can occur, i.e. (1) non-radiative via deep level; (2) Auger recombination; (3) Surface recombination. We will introduce them superlatively.
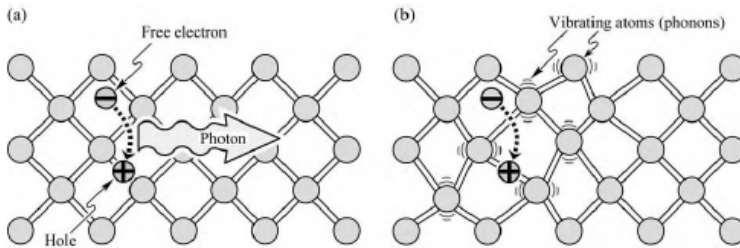

Figure 2.7: (a) Radiative recombination of an electron-hole pair accompanied by the emission of a photon with energy $hv \approx E_g$. (b) In non-radiative recombination evens, the energy released during the electron-hole recombination is converted to phonons.

(i) Non-radiative via deep level

Defects in the crystal structure are the most common cause for non-radiative recombination. These defects include unwanted foreign atoms, native defects, dislocations, and any complexes of defects, foreign atoms, or dislocations. In compound semiconductors, native defects include interstitials, vacancies, and antisite

defects. All such defects have energy level structures that are different from substitutional semiconductor atoms. It is quite common for such defects to form one or several energy levels within the forbidden gap of the semiconductor.

Energy levels within the gap of the semiconductor are efficient recombination centers; in particular, if the energy level is close to the middle of the gap. The recombination of carriers via a trap level is shown schematically in Figure 2.8 (a). Owing to the promotion of non-radiative processes, such deep levels or traps are called *luminescence killers*.

(ii) Auger recombination

The energy is given to a third carrier, which is excited to a higher energy level without moving to another energy band. After the interaction, the third carrier normally loses its excess energy to thermal vibrations. The recombination of carriers via Auger process is shown schematically in Figure 2.8 (b). Since this process is a three-particle interaction, it is normally only significant in non-equilibrium conditions when the carrier density is very high. The Auger generation process is not easily produced, because the third particle would have to begin the process in the unstable high-energy state.
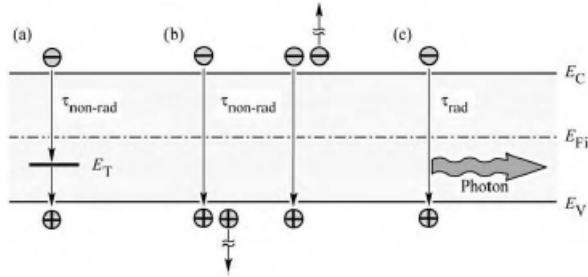

Figure 2.8: Band diagram illustrating recombination: (a) non-radiative via deep level; (b) non-radiative via Auger process and (c) radiative.

(iii) Surface recombination

Substantial non-radiative recombination can occur at semiconductor surfaces. Surfaces are a strong perturbation of the periodicity of a crystal lattice. Recall that the band diagram model is based on the strict periodicity of a lattice. Since this periodicity ends at a surface, the band diagram will need to be modified at a semiconductor surface. This modification includes the addition of electronic states within the forbidden gap of the semiconductor.

The semiconductor surface will be considered from a chemical point of view. Atoms at the surface cannot have the same bonding structure as bulk atoms due to the lack of neighboring atoms. Thus some of the valence orbitals do not form a chemical bond. These partially filled electron orbitals, or *dangling bonds*, are electronic states that can be located in the forbidden gap of the semiconductor where they act as recombination centers. Depending on the charge state of these valence orbitals, the states can be acceptor-like or donor-like states.

The dangling bonds may also rearrange themselves and form bonds between neighboring atoms in the same surface plane or absorb the chemical groups in the extrinsic environment to build the new bonds. These *surface reconstructions* can lead

to a locally new atomic structure with state energies different from bulk atomic states. The surface bonding structure depends on the specific nature of the semiconductor surface. The energetic location of surface states is very difficult to predict, even with powerful theoretical models. Thus phenomenological models of surface recombination are commonly used. It has been shown that electronic states within the forbidden gap appear at semiconductor surfaces. Bardeen and Shockley (Shockley, 1950) pioneered the understanding of surface states and their role as recombination centers.

The effect of surface recombination on the carrier distribution in a p-type semiconductor subjected to illumination can be calculated. Assume that the illumination causes a uniform steady state generation rate G. The one-dimensional continuity equation must be fulfilled at any point in the semiconductor. The continuity equation for electrons is given by

$$\frac{\partial \Delta n(x,t)}{\partial t} = G - R + \frac{1}{e}\frac{\partial}{\partial x}J_n \tag{2.1}$$

where J_n is the current density caused by electrons flowing to the surface. In the bulk of the uniform semiconductor, there is no dependence on space and thus the continuity equation reduces to $G = R$ under steady-state conditions. Using the recombination rate in the bulk as given by Eq. (2.2), the excess carrier concentration

$$\frac{d}{dt}\Delta n(t) = -\frac{\Delta n(t)}{\tau_n} \tag{2.2}$$

in the bulk is given by $\Delta n_\infty = G\tau n$ as indicated in Fig. 2.9. Assuming that the electron current is a diffusion current of the form

$$J_n = eD_n \frac{\partial \Delta n(x,t)}{\partial x} \tag{2.3}$$

and inserting the diffusion current into Eq.(2.1) yields the continuity equation for diffusive currents, i.e.

$$\frac{\partial \Delta n(x,t)}{\partial t} = G - \frac{\partial n(x,t)}{\tau_n} + D_n \frac{\partial^2 \Delta n(x,t)}{\partial x^2} \tag{2.4}$$

At the semiconductor surface, carriers will recombine rapidly due to surface states. The **boundary condition** at the surface is given by

$$eD_n \frac{\partial \Delta n(x,t)}{\partial x}\bigg|_{x=0} = eS\Delta n(x,t)\big|_{x=0} \tag{2.5}$$

where S is the surface recombination velocity. The boundary condition states that minority carriers diffusing to the surface will recombine at the surface. We assume that the generation rate is constant with time, and thus the minority carrier concentration has no time dependence. The steady-state solution to the differential equation with the above boundary condition is given by

$$n(x) = n_0 + \Delta n(x) = n_0 + \Delta n_\infty \left[1 - \frac{\tau_n S exp(-x/L_n)}{L_n + \tau_n s} \right] \qquad (2.6)$$

The carrier concentration near a semiconductor surface is shown in Fig. 2.9 for different surface recombination velocities. For $S \rightarrow 0$, the minority carrier concentration at the surface is identical to the bulk value, i.e. $n(0) \rightarrow n_0 + \Delta n_\infty$. For $S \rightarrow \infty$, the minority carrier concentration at the surface approaches the equilibrium value, i.e. $n(0) \rightarrow n_0$.

The surface recombination velocities for several semiconductors are summarized in Table 2.1. The data shown in the table show that GaAs has a particularly high surface recombination velocity.
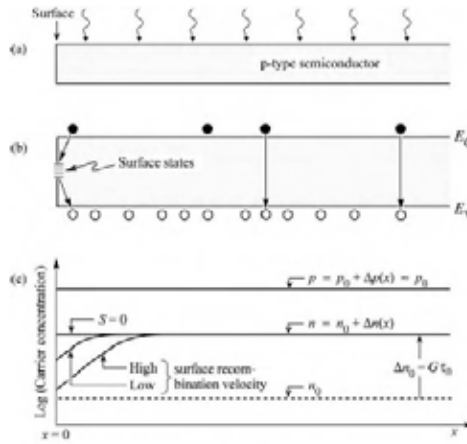

Firgure 2.9: (a) Illuminated p-type semiconductor, (b) band diagram, and (c) minority and majority carrier concentrations near the surface assuming uniform carrier generation due to illumination. The excess carrier concentrations are Δn and Δp.

Table 2.1. Surface recombination velocities of several semiconductors

Semiconductor	Surface recombination velocity
GaAs	$S = 10^6$ cm/s
GaN	$S = 5 \times 10^4$ cm/s
InP	$S = 10^3$ cm/s
Si	$S = 10^1$ cm/s

Surface recombination leads to a reduced luminescence efficiency and also to heating of the surface due to non-radiative recombination at the surface. Both effects are unwanted in electroluminescent devices.

Chapter 3

Sample preparation and characterization techniques

As mentioned in the first Chapter, ZnO is a versatile functional material. It has a rich family of nanostructures such as nanotubes, nanowires, nanorods, nanobelts, nanocables, and nanoribbons so on which can be fabricated by different techniques (see Figure 3.1[64]). In this work, we only choose chemical bath deposition (CBD) to realize the size controllable growth of ZnO nanorods and use optical spectroscopy to investigate their structure and optical properties. Therefore, this chapter will be divided into two sections: sample preparation and characterization techniques.
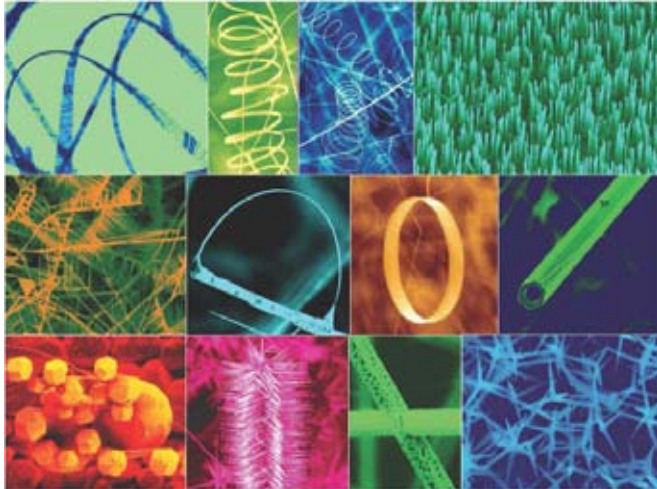

Figure 3.1: Different morphologies of ZnO nanostructures

3.1 Sample preparation

In recent years low-temperature wet chemical methods have received more and more attention and now already been commonly used to grow ZnO nanostructures. There are mainly three common approaches in chemical growth at low temperature, i.e. the hydrothermal, chemical bath deposition (CBD), and electrochemical deposition. At here, we only choose CBD method to grow samples. One of its major advantages is that the growth temperature can be as low as $50^{o}C$. With such low temperature, much cheaper substrates such as plastic and glass can be used. And also there is a possibility to use p-type polymer as the p-type substrate when producing pn-junctions from ZnO nanorods, since the ZnO nanorods are n-type.

One problem is urgent to be solved for CBD method is that the nanorods grown on Si substrate show a poor reproducibility, difficulty to control size and bad orientation. Until now, the most successful approach for the CBD is growing ZnO nanorods on pretreated substrate, i.e. two-step CBD method [65-68]. Among those pretreated methods, thermal deposition [66], radio frequency magnetron-sputtering [67] and spin coating [68] techniques were usually applied to prepare ZnO seed layer on substrates. Clearly, the latter is much more easily carried out and the process is more economical. Therefore, we select spin coating technique to introduce seeding layer on substrates and use CBD method to grow ZnO nanorods.

During the process of two-steps CBD, there are many parameters can be changed which will influence the structure and morphology of the sample. In this study, a few of them were investigated (see paper I). The parameters changed in this study are listed as follows:

- Seed layer
- pH value of chemical solution
- Angel θ between substrate and beaker bottom
- Growth time

After the systematical investigation, the optimized growth conditions to grow ZNAs were summarized out as follows: seed layer of ZnO nanoparticles, pH=6 and $\theta=70°$. On the basis of it, we found an effective way to control the size of well-aligned ZNAs (see paper II).

In our experiments, all chemicals were analytical reagent grade and used without further purification. All the aqueous solutions were prepared using distilled water. Si (100) substrates were ultrasonically cleaned for 15min in ethanol before spin coating.

3.1.1 Substrate pre-treatment

Three different seed layers were chosen in our work, i.e. ZnO powder, Zn powder and ZnO nanoparticles. According to the seed layer of ZnO powder and Zn powder, the 0.005M suspension ethanol solution was prepared by ultrasonic technique and spin coated onto the solution for 4 times. The spin speed is 2000rpm and the spin time is 30s. And then the substrates were put into the oven for heating under $100^{o}C$ for 10min in order to keep the seeds sticking onto substrates. For the seed layer of ZnO nanoparticles, zinc acetate dihydrate (Zn $(C_2H_3O_2)_2·2H_2O$) was dissolved in the pure ethanol with concentration of 5mM. This solution was coated for several times onto Si (100) substrates by a spin coater (Laurell WS-400-8TFW-Full) at the rate of 2000 rpm for 30s. The coated substrates were dried in room temperature and then annealed in air at 250°C for 30min. The annealed temperature of 250°C is a little above the decomposition temperature of zinc acetate particles in order to form ZnO nanoparticles seed layer. In the following, all substrates were pretreated twice for the above processes before final growth of ZnO nanorods.

Figure 3.2 shows the low and high magnification SEM images of the sample grown on the Si substrate with different seed layer. Compared with the sample bare Si, the seed layer of ZnO powder only makes the sample with higher density and the alignment is almost same. The seed layer of Zn powder makes the morphology of sample shows the flower shape. Only the sample grown on the Si substrate with the seed layer of ZnO nanoparticles has the best alignment and smallest diameter. The detail analysis of how the seed layer of ZnO nanoparticles affect the orientation can be found in paper I.
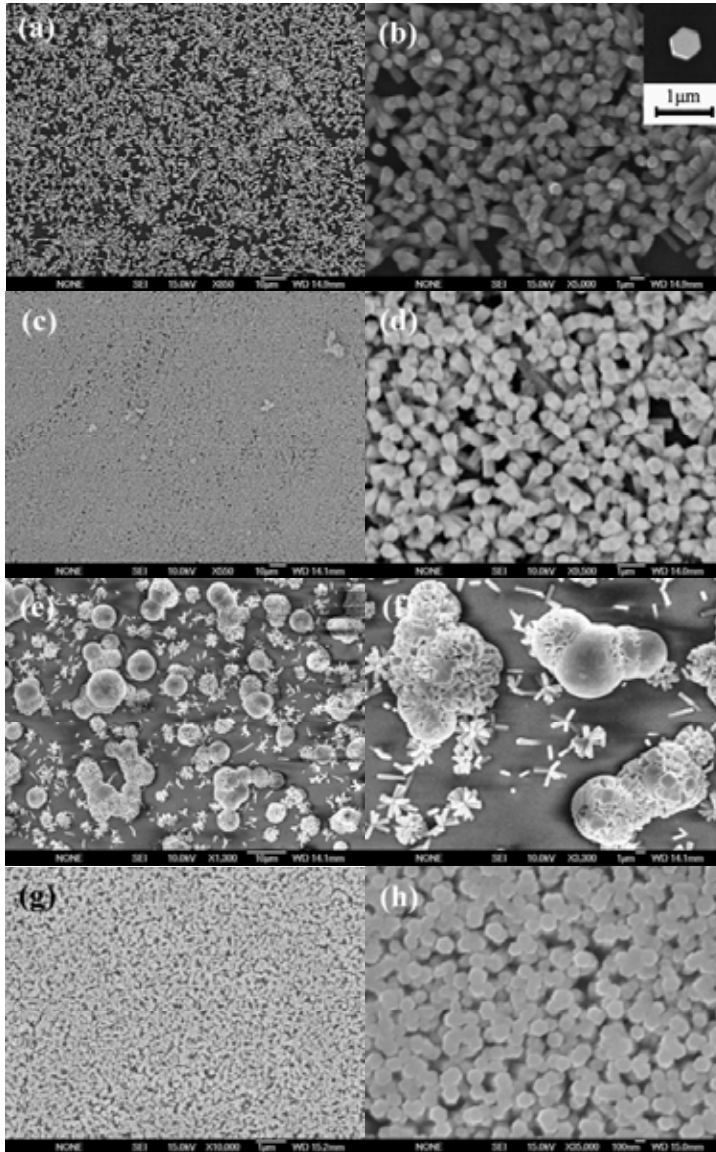
Figure 3.2: The low and high magnification SEM images of the sample grown on the Si substrate with different seed layer. (a)(b) bare Si; (c)(d)ZnO powder; (e)(f)Zn powder; (g)(h) ZnO nanoparticles.

As a summary, the seed layer of ZnO nanoparticles is the most beneficial one for the growth of well-aligned ZNAs with small diameter. The study of other growth parameters changed can be found in paper I. The density of ZnO nanoparticles on the substrate can be controlled by the number of spin times, which can be used to control the size of ZNAs. The detailed processes and controllable mechanism have been described in paper II.

3.1.2 CBD growth

For CBD growth process, the aqueous solutions of zinc nitrate hexahydrate [Zn $(NO_3)_2.6H_2O$, 99.9% purity] and methenamine ($C_6H_{12}N_4$, 99.9% purity) were first prepared respectively and then were mixed together. The concentrations of both were fixed at 0.1M. The pretreated Si substrates were immersed into the aqueous solution and tilted against the wall of beaker. The angel between substrate and beaker bottom is ~70˚. Then the beaker was put into the oven and kept in it for 2h at a constant temperature of 93°C. After growth, the substrate was removed from the solution, rinsed with deionized water and then dried at room temperature.

3.1.3 Annealing

For as-grown ZnO nanorods arrays (ZNAs), a post-growth thermal treatment was performed at 500°C, 600 °C and 700 °C respectively for 1h in air atmosphere and then quenched to room temperature by removal from the oven. This process is normally used to change the material properties.

3.2 Characterization techniques

After the preparation of the samples, different characterization techniques were used to investigate their structure and optical properties. Scanning electron microscope (SEM) was used to get the morphology of the samples. An atomic force microscope (AFM) was utilized to detect the morphology of pretreated substrates. The detailed information about the structure of the samples can be obtained from XRD measurement. The optical properties were investigated by micro-photoluminescence (PL), micro-Raman scattering, and resonant Raman scattering (RRS) measurements. The surface effect versus the diameter of the ZnO nanorods were studied by means of time resolved photoluminescence (TRPL). In this section, we will briefly introduce all the techniques.

3.2.1 Scanning electron microscope

The scanning electron microscope (SEM) is a type of electron microscope that images the sample surface by scanning it with a high-energy beam of electrons in a raster scan pattern. The electrons interact with the atoms to make the sample producing signals that contain information about the sample's surface topography, composition and other properties such as electrical conductivity. The types of signals produced by an SEM include secondary electrons, back scattered electrons (BSE), characteristic x-rays, light (cathodoluminescence), specimen current and transmitted electrons. These types of signal all require specialized detectors for their detection that are not usually all present on a single machine.
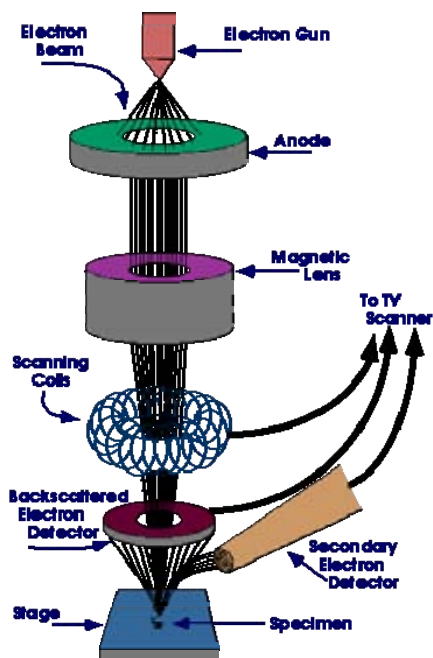
Figure 3.3: Schematic image of SEM

The schematic image of SEM is illustrated in Figure 3.3 in order to show how it works. The SEM uses electrons instead of light to form an image. A beam of electrons is produced at the top of the microscope by heating of a metallic filament. The electron beam follows a vertical path through the column of the microscope. It makes its way through electromagnetic lenses which focus and direct the beam down towards the sample. Once it hits the sample, other electrons such as backscattered or secondary are ejected from the sample. Detectors collect the secondary or backscattered electrons, and convert them to a signal that is sent to a viewing screen similar to the one in an ordinary television, producing an image.

To characterize the as-grown ZnO nanostructures, a JEOL JSM-6301F scanning electron microscope was used in our experiments. The chamber pressure is about 10^{-6} mbar. The gun voltage is 15kV. A max resolution of about 10nm can be achieved. Figure 3.4 gives the typical SEM images of our sample.

The SEM gives information on the morphology of the surface of the sample, which implies that is possible to determine if any growth has taken place. However, the images from the SEM are not a definitive proof that obtained nanostructures actually consists of ZnO. Even though the SEM produces 3D images they give no information regarding the exact atomic structure of the sample. The 3D images are easy to interpret and they reveal topographic features of the sample. The SEM images allow us to examine the diameter, length, shape and density of the ZnO nanostructures.
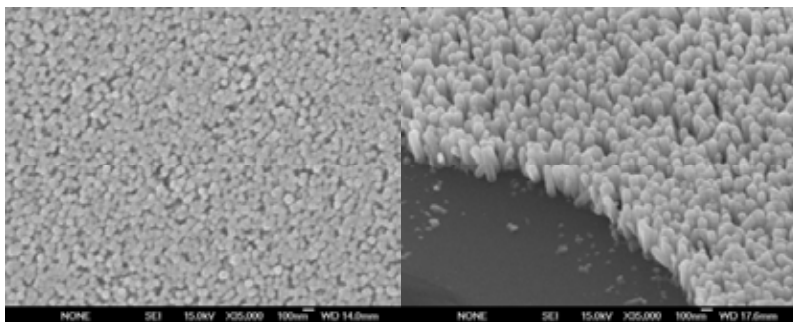
Figure 3.4: Typical SEM images of ZnO nanorod arrays. Left is image of top view, Right is cross sectional image observed from 45°.

3.2.2 X-ray diffraction

X-rays are electromagnetic radiation of wavelength about 1 Å (10^{-10} m), which is about the same size as an atom. They occur in that portion of the electromagnetic spectrum between gamma-rays and the ultraviolet. The discovery of X-rays in 1895 enabled scientists to probe crystalline structure at the atomic level.

When X-rays interact with a crystalline substance (phase), one gets a diffraction pattern. About 95% of all solid materials can be described as crystalline. Each crystalline solid has its unique characteristic X-ray diffraction (XRD) pattern which may be used as a "fingerprint" for its identification. Today about 50,000 inorganic and 25,000 organic single components, crystalline phases, and diffraction patterns have been collected and stored on magnetic or optical media as standards.
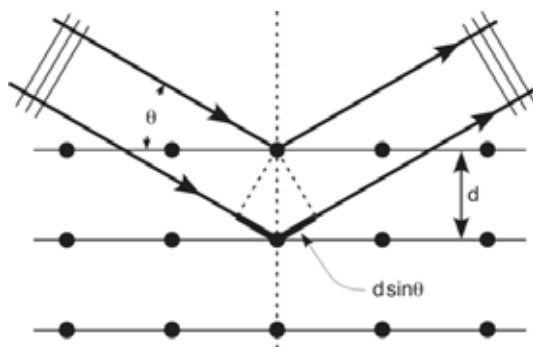

Figure 3.5: Reflection of x-rays from two planes of atoms in a solid.

Figure 3.5 illustrates the reflection of x-rays from two planes of atoms in a solid. A crystal lattice is a regular three-dimensional distribution (cubic, rhombic, etc.) of atoms in space. These are arranged so that they form a series of parallel planes separated from one another by a distance d, which varies according to the nature of the material. For any crystal, planes exist in a number of different orientations - each with its own specific d-spacing. When a monochromatic X-ray beam with wavelength lambda is projected onto a crystalline material at an angle theta, diffraction occurs only when the distance traveled by the rays reflected from successive planes differs by a complete number n of wavelengths, which leads to famous Bragg's Law:

$$n\lambda = 2d\sin(\theta) \qquad (3.1)$$

where *n* is an integer 1,2,3…..(usually equal 1), λ is wavelength in angstroms (1.54 Å for copper), d is interatomic spacing in angstroms, and θ is the diffraction angle in degrees. By varying the angle theta, the Bragg's Law conditions are satisfied by different d-spacing in polycrystalline materials. Plotting the angular positions and intensities of the resultant diffracted peaks of radiation produces a pattern, which is characteristic of the sample. Where a mixture of different phases is present, the resultant diffractogram is formed by addition of the individual patterns. Based on the principle of X-ray diffraction, a wealth of structural, physical and chemical information about the material investigated can be obtained.

XRD has been in use in two main areas, for the fingerprint characterization of crystalline materials and the determination of their structure. Once the material has been identified, X-ray crystallography may be used to determine its structure, i.e. how the atoms pack together in the crystalline state and what the interatomic distance and angle are etc. X-ray diffraction is one of the most important characterization tools used in solid state chemistry and materials science. We can determine the size and the shape of the unit cell for any compound most easily using the diffraction of x-rays.
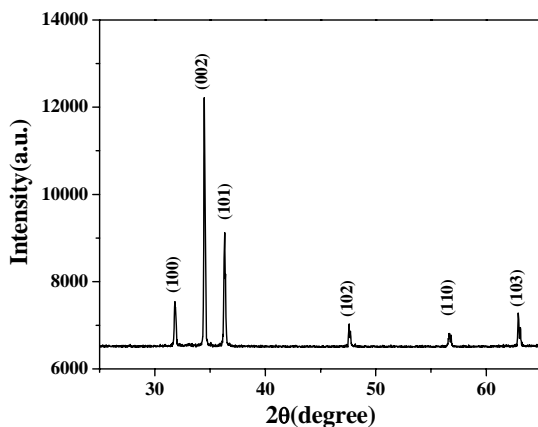

Figure 3.6: Typical XRD pattern of ZnO nanorods.

Zn O
Zinc Oxide
Ref: Calculated from ICSD using POWD-12++, (1997)
Ref: Garcia-Martinez, O et al., Solid State Ionics, 63, 442 (1993)

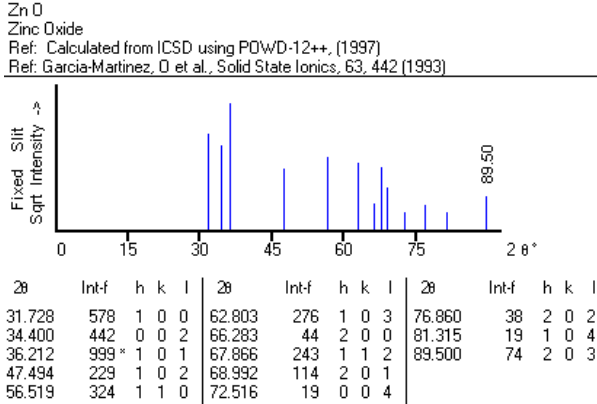| 2θ	Int-f	h	k	l	2θ	Int-f	h	k	l	2θ	Int-f	h	k	l
31.728	578	1	0	0	62.803	276	1	0	3	76.860	38	2	0	2
34.400	442	0	0	2	66.283	44	2	0	0	81.315	19	1	0	4
36.212	999 *	1	0	1	67.866	243	1	1	2	89.500	74	2	0	3
47.494	229	1	0	2	68.992	114	2	0	1					
56.519	324	1	1	0	72.516	19	0	0	4					

Figure 3.7: Standard JCPDS card of bulk ZnO with hexagonal structure

Figure 3.6 shows the typical XRD pattern of our sample. All the peaks of the XRD patterns can be indexed to ZnO with the hexagonal wurtzite structure. In comparison with the standard card of bulk ZnO with hexagonal structure (see Figure 3.7), no diffraction peaks of other impurities are detected, which testify that the substance deposited on the substrates only belongs to ZnO.

3.2.3 Atomic force microscope

The atomic force microscope (AFM) is a very high-resolution type of scanning probe microscope, with demonstrated resolution of fractions of a nanometer, more than 1000 times better than the optical diffraction limit. Binnig, Quate and Gerber invented the first AFM in 1986. The AFM is one of the foremost tools for imaging, measuring and manipulating matter at the nanoscale. The term 'microscope' in the name is actually a misnomer because it implies looking, while in fact the information is gathered by "feeling" the surface with a mechanical probe. Piezoelectric elements that facilitate tiny but accurate and precise movements on (electronic) command enable the very precise scanning.

Figure 3.8 illustrates the block diagram of AFM. The AFM consists of a microscale cantilever with a sharp tip (probe) at its end that is used to scan the specimen surface. The cantilever is typically silicon or silicon nitride with a tip radius of curvature on the order of nanometers. The AFM works by scanning a fine ceramic or semiconductor tip over a surface much the same way as a phonograph needle scans a record. When the tip is brought into proximity of a sample surface, Van der Waals forces between the tip and the sample lead to a deflection of the cantilever. The magnitude of the deflection is captured by a laser that reflects at an oblique angle from the very end of the cantilever. A plot of the laser deflection versus tip position on the sample surface provides the resolution of the hills and valleys that constitute the topography of the surface. The AFM can work with the tip touching the sample (contact mode), or the tip can tap across the surface (tapping mode) much like the cane of a blind person.
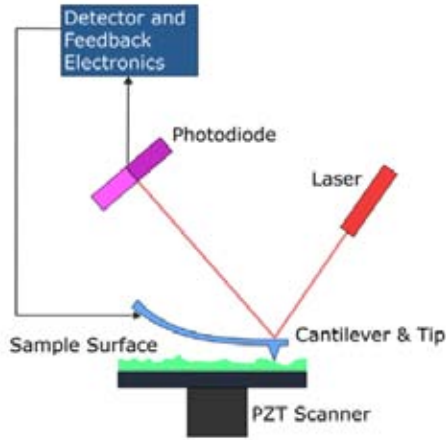
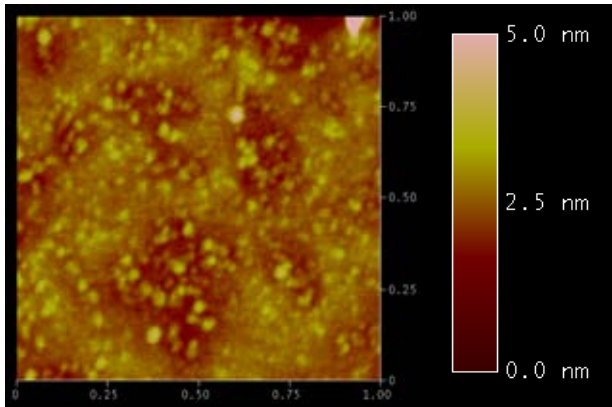Figure 3.8: Block Diagram of Atomic Force Microscope

Figure 3.9: The 1μm×1μm AFM image of the pretreated substrates.

Compared with SEM, AFM provides extraordinary topographic contrast direct height measurements and unobscured views of surface features. Figure 3.9 shows the 1μm×1μm AFM image of the pretreated substrates. From this image, it can be seen that the dispersion of ZnO nanoparticles is relatively uniform in the comparison with the nuclei formed on the bare substrates, and the average diameter and height of ZnO nanoparticles on the substrates is about 20nm and 3.5nm respectively. In the comparison between the SEM images of ZnO nanorods and the AFM images of pre-treated Si substrates, the relationship between the sample and seed layer is able to be revealed, which will be described in Paper II.

3.2.4 Raman Spectroscopy

Raman scattering is a powerful light scattering technique used to diagnose the internal structure of molecules and crystals. In a light scattering experiment, light of a known frequency and polarization is scattered from a sample. The scattered light is then analyzed for frequency and polarization. Raman scattered light is frequency-shifted with respect to the excitation frequency, but the magnitude of the shift is independent of the excitation frequency. This "Raman shift" is therefore an intrinsic property of the sample.
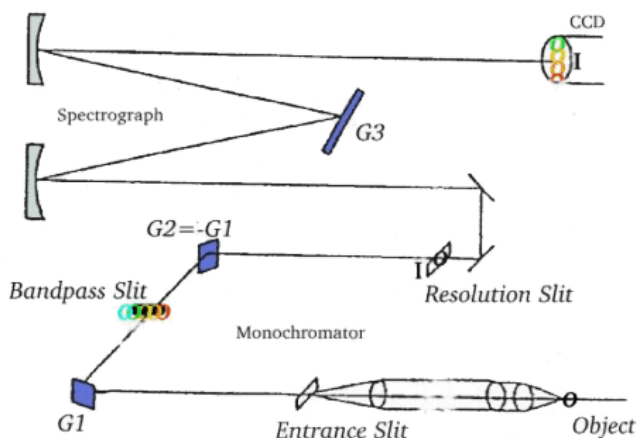

Figure 3.10 Schematic images of Raman spectrometer

Raman spectroscopy usually consists of three parts: Laser, spectrometer and charge-coupled device array (CCD) detector. The spectrometer itself is a commercial "triple-grating" system. Physically, it is separated into two stages, i.e. monochromator and spectrograph, which are shown schematically in Figure 3.10. The laser beam from the laser is filtered for monochromatic and directed by a system of mirrors to a focusing/collecting lens. The beam is focused onto the sample; the scattered light which passes back through the same lens is then passed through a second lens into the monochromator of the spectrometer. Finally the light is refocused and sent out to the spectrograph of the spectrometer to focus the filtered light on the final grating. The dispersed light is now analyzed as a function of position, which corresponds to wavelength. The signal as a function of position is read by the system detector. In the present case the detector is a multichannel charge-coupled device array (CCD) in which the different positions (wavelengths) are read simultaneously. The wavelength/intensity information is then read to a computer and converted in software to frequency/intensity. This is the Raman spectrum which appears as the raw data.

Wurtzite ZnO belongs to $C_{6v}{}^{4}$ (*P63mc*) space group, with two formula units per primitive cell. At the point of the Brillouin zone, group theory predicts the existence of the following phonon modes: $\Gamma = 2A_1 + 2 B_1 + 2E_1 + 2E_2$. Among these modes, there

23

are acoustic modes with $\Gamma_{aco} = A_1 + E_1$ and optical modes with $\Gamma_{opt} = A_1 + 2\,B_1 + E_1 + 2$ E_2. The B_1 modes are silent modes. For the long-range electrostatic forces, both A_1 and E_1 modes are polar and are split into transverse (TO) and longitudinal optical (LO) phonons, all being Raman and infrared active. The A_1 phonon vibration is polarized parallel to the C-axis; the E_1 phonon is polarized perpendicular to the C-axis. The two E_2 modes (E^{high}_2, E^{low}_2) are nonpolar modes and are Raman active only. Every mode corresponds to a band in the Raman spectrum. Figure 3.11 illustrates the room temperature Raman spectrum of ZnO single crystal. All the modes of ZnO can be seen from this figure. The intensity of these bands depends on the scattering cross section of these modes. For the polar modes, the scattering cross section of TO modes on only the deformation potential, but the LO modes depend, in addition, on the linear optoelectric effect. The linear optoelectric effect is attributed to polar phonon-induced macroscopic electric field coupled with excited electrons (Fröhlich interaction).
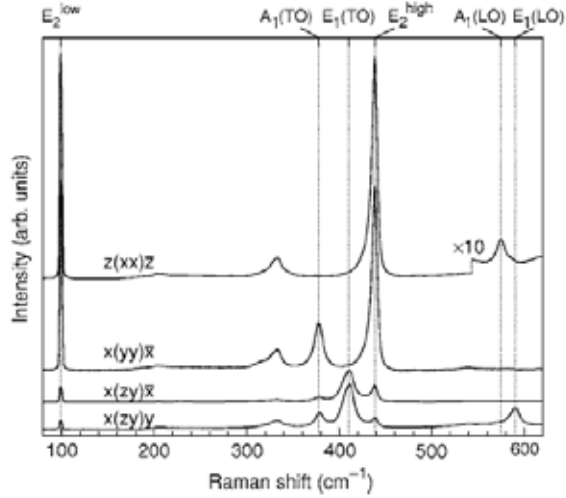

Figure 3.11:   Room temperature first-order Raman spectra of ZnO in scattering geometries corresponding to $A_1 + E_2$ and E_1 symmetries.

The conventional micro-Raman spectra in our experiments have been collected in a confocal backscattering configuration under the 100x objective of an Olympus microscope. The 514.5nm line of a CW Ar-Kr-ion laser, Spectra Physics 2060, with a power of 5mW at the sample position, was used as probe. The cross-polarized scattered radiation was filtered by the first two stages of a triple grating Dilor XY 800 spectrometer, arranged in the subtractive configuration, to remove the strong elastic component, dispersed by the third stage, and recorded by a liquid nitrogen cooled CCD camera, Wright Instruments. Figure 3.12 presents the typical Raman spectrum of as-grown ZnO nanorod arrays with 90nm diameter.
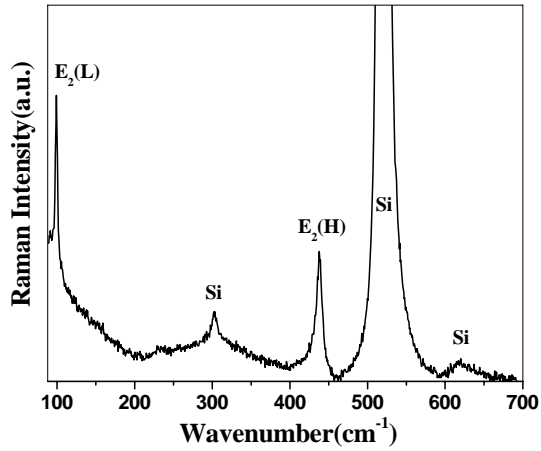
Figure 3.12 Typical Raman spectrum of the as-grown ZnO nanorods array with 90nm diameter.
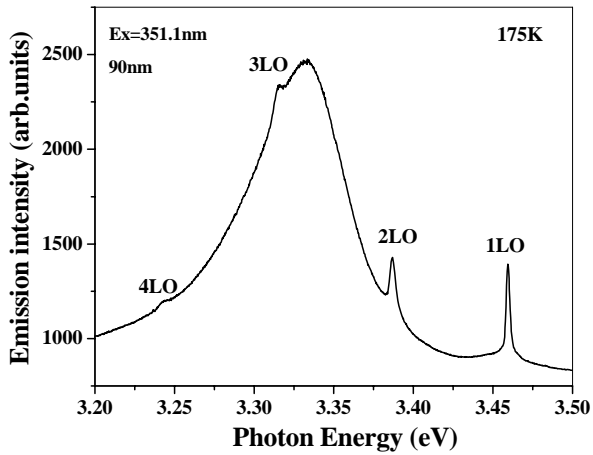

Figure 3.13 Resonant Raman spectrum of as-grown ZnO nanorod arrays with 90nm diameter measured at the temperature of 175K.

To study the low-dimensional ZnO by Raman spectroscopy, the resonance condition is usually necessary due to two advantages as follows. On one hand, the scattering cross sections of LO modes are larger than those of the TO, so in the Raman spectra the intensity of LO bands are remarkably higher than that of the TO bands. Therefore, LO bands are better candidates for investigating samples. However, the LO modes can be affected easily by other elementary excitation in the samples or external disturbances, and then their energy decreases. So, in the typical Raman spectra, the LO band has a low-energy tail. This broad line-shape will affect the discussion of the angular dispersion of LO phonon. To study the LO band, it is necessary to get rid of these disturbances. Fröhlich interaction, which contributes to the scattering cross-section of LO phonon, is sensitive to resonance condition. Most of the disturbances are not sensitive to the resonance condition. In the resonance Raman spectra, only the LO modes and their overtones can be enhanced. So it can be assumed that in the resonance Raman spectra bands of LO and its overtones are pure superpositions of A_1-LO and E_1-LO modes.

In resonance Raman spectroscopy, the energy of the incoming laser is adjusted such that it or the scattered light coincides with an electronic transition of the molecule or crystal. For ZnO, a laser line with 351.1nm was used in our measurement. Figure 3.13 presents the resonant Raman spectrum of as-grown ZnO nanorod arrays with 90nm diameter. Four order of LO phonon lines can be seen from the sample.

3.2.5 Photoluminescence Spectroscopy

Photoluminescence (PL) is the spontaneous emission of light from a material under optical excitation. The excitation energy and intensity can be chosen to probe different excitation types and also different parts of the sample. PL analysis is nondestructive. The technique requires very little sample manipulation or environmental control. When light of sufficient energy is illuminated a material, photons are absorbed and (electronic) excitations are created. These excitations relax and emit a photon. The PL can be collected and analyzed to provide information about the photo-excited states. The PL spectrum reveals transition energies and the PL intensity gives a measure of the relative rates of radiative and non-radiative recombination. Variation of the PL intensity upon change of external parameters, e.g., temperature, excitation energy, power of excitation, can be used to further characterize electronic states and bands.

PL investigations can be used to characterize a variety of materials parameters, which will be introduced respectively as follows:

(1) Band gap determination

The most common radiative transition in semiconductors is between states in the conduction and valence bands - bandgap of a semiconductor. Bandgap determination is particularly useful when working with new compound semiconductors.

(2) Impurity levels and defect detection

Radiative transitions in semiconductors also involve localized defect levels. The PL energy associated with these levels can be used to identify specific defects, and the PL intensity can be used to determine their concentration.

(3) Recombination mechanisms

As discussed above, the return to equilibrium, also known as "recombination" can involve both radiative and nonradiative processes. The PL intensity and its dependence on the level of photo-excitation and temperature are directly related to the

dominant recombination process. Analysis of PL helps to understand the underlying physics of the recombination mechanism.

(4) Material quality

In general, nonradiative processes are associated with localized defect levels, whose presence is detrimental to material quality and subsequent device performance. Thus, material quality can be measured by quantifying the amount of radiative recombination.

The typical PL experimental set-up is illustrated in Figure 3.14. The samples were excited using a continuous-wave (cw) laser operating, or a tunable Optical Parametric Oscillator (OPO) laser system, producing pulses excitation. The luminescence was resolved with a monochromator and detected by a high sensitivity germanium detector (Edinburgh Instruments) or a Hamamatsu R5509-72 InP/InGaAs nitrogen-cooled photomultiplier tube.
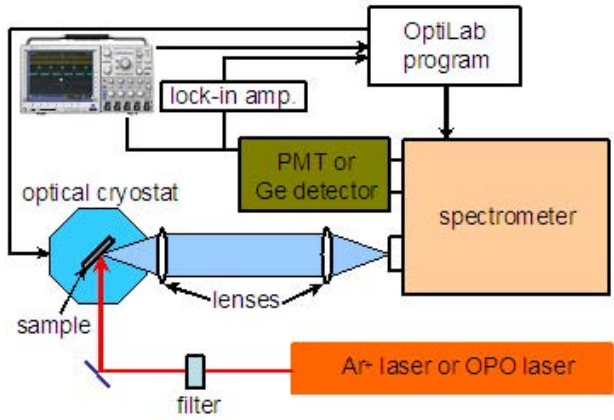

Figure 3.14: Typical experimental set-up for PL measurements.

In our measurement, the PL experiments were carried out in a variable temperature continuous-flow cryostat accessing the 1.5-300 K range. A CCD detector (Spectrum One) and monochromator HR460 from Jobin Yvon-Spex were used to disperse and detect the ZnO emission. Laser line with a wavelength of 266 nm from a diode laser (Coherent Verdi) pumped resonant frequency doubling unit (MBD 266) was used as excitation source. The PL spectrum of ZnO nanorod arrays is illustrated in Figure 3.15.

Under pulsed excitation, PL intensity transients yield lifetime of excited state, which is usually called Time-resolved PL (TRPL). TRPL is a nondestructive and powerful technique commonly used for the optical characterization of semiconductors. The free-carrier or exciton lifetime, an important parameter related to material quality and device performance, can be measured by TRPL spectroscopy. The exciton lifetimes will vary with crystal quality, becoming longer as the quality improves. The efficiency of the radiative recombination is strongly related to the decay time of the particular transition. In addition, thermally activated processes of non-radiative recombination cause changes of PL and can be investigated in this way.
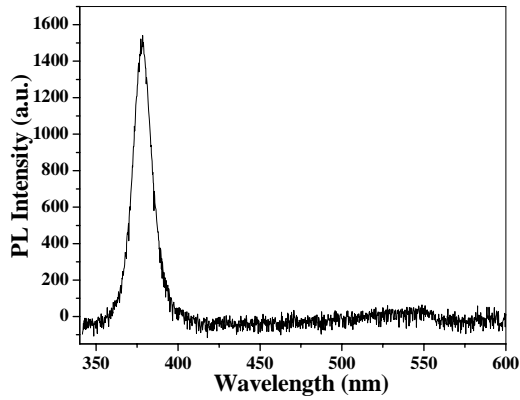
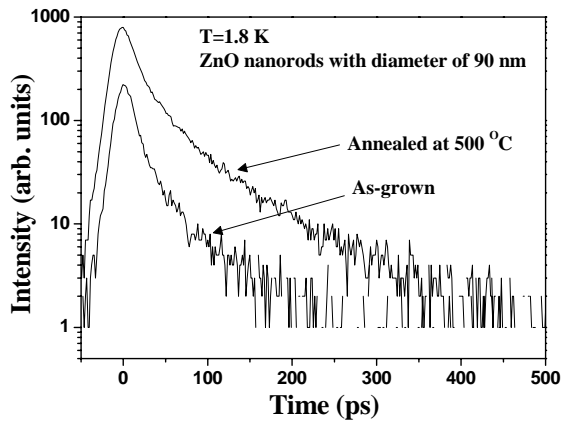Figure 3.15: The PL spectrum of ZnO nanorod arrays growth with CBD method.

Figure 3.16: Decay curves for 90 nm diameter ZnO nanorods from as-grown sample and after annealing at 500°C for 1h. The decays were measured at 1.8 K.

TRPL was also performed in our experiment by using an excitation laser line from a frequency tripled sapphire:Ti laser emitting at 266 nm, a 0.3 m monochromator and a streak camera at 1.8 K. The TRPL spectra of ZnO nanorod arrays are illustrated in Figure 3.16.

Chapter 4

Conclusion and outlook

The synthesis and optical properties of ZnO nanorod arrays (ZNAs) were investigated in detail in this thesis. Paper I and Paper II provide an effective way to grow vertically well-aligned ZNAs on Si substrates by a two-steps chemical bath deposition method (CBD), i.e. substrate pretreatment with spin coating to form ZnO nanoparticles layer and CBD growth. Paper III and Paper IV describe the effect of post-annealing on the structure and optical properties of ZNAs. The main result of each paper will be given as follows.

Starting with Paper I, optimized growth conditions to fabricate well-aligned ZNAs on Si substrates have been obtained in two-step CBD method. The results show that substrate pretreatment, angel (θ) between substrate and beaker bottom and growth time (t) indeed have great influence on the growth of ZNAs, and their influence mechanisms have been respectively explained in detail. The introduction of a ZnO nanoparticle layer on the substrate not only helps to decrease the diameter but also has a strong impact on the orientation of ZNAs. Under the growth condition of pH=6, θ=70˚ and t=2h, the well-aligned ZnO nanorod arrays with 50nm diameter was obtained on the pretreated Si substrates. As-synthesized ZnO nanorods have a perfect crystallization and low density of deep level defects due to only a strong UV peak at 385 nm appears in room temperature PL spectrum for this sample.

In Paper II, on the basis of Paper I, the diameter of well-aligned ZnO nanorod arrays (ZNAs) grown on Si substrates has been well controlled from 150nm to 40nm by two-step CBD. The effects of ZnO nanoparticles density and diameter on size and alignment of ZNAs were investigated in detail. In the comparison between the SEM images of ZnO nanorods and the AFM images of pre-treated Si substrates, the relationship between the sample and seed layer is able to be revealed. The results indicate that both diameter and density of ZnO nanoparticles will influence the size and alignment of ZNAs, but the density will play a key role to determine the diameter of ZNAs when the density is higher than the critical value of 2.3×10^8cm^{-2}.

In Paper III, the effects of annealing temperature on the structure and optical properties of ZNAs were investigated in detail. The results clearly indicated that the post-thermal treatment at 500°C in the air resulted in the CBD grown ZNAs with good crystal structure and good optical properties due to the decrease of surface defects. We also utilized Raman spectroscopy and low temperature PL measurements to identify, for the first time to the best of our knowledge, the surface defect contribution and outgoing resonant effect in RRS, which indicated that the Raman measurements can be used to monitor the change of surface defects and deep level defects in the CBD grown ZNAs under thermal treatment from 500°C to 700°C.

In Paper IV, as discussed in Paper III, the surface defects indeed existed in the ZNAs, therefore, surface recombination may be play a great role in the optical properties of ZNAs. In order to testify it, the optical properties of the grown ZnO

nanorods were investigated by a time-resolved photoluminescence spectroscopy. Three samples containing ZnO nanorods on Si (001) substrates with the diameter of 150, 90 and 60 nm, respectively, were used in this study. The results found that the effective decay time of the near bandgap recombination in the CBD grown ZnO nanorods strongly depends on the diameter of the ZnO nanorods. Typically, the decay curves obtained from these ZnO nanorods show a combination of two exponential decays. The experimental results show that the fast exponential decay is related to surface recombination and the slow decay is related to the "bulk" decay. The measured decay time of the effective surface recombination decreases with decreasing the diameter, while the "bulk" decay time remains unchanged. The results also show that an annealing treatment around $500^{o}C$ significantly reduces the surface recombination rate. A simple carrier and exciton diffusion equation is also used to determine the surface recombination velocity, which results in a value between 1.5 and 4.5 nm/ps.

Our results in Paper I and Paper II offer an effective way to solve the existing problems, such as reproducibility, size control and orientation of ZANs, in CBD methods. Therefore, this study can not only provides a method for large-scale fabrication of ZnO nanorods with a low cost, but also open a way to the size-controlled fabrication of other materials by a hydrothermal approach. While the results in Paper III and Paper IV, the results of our investigation provide an effective way to improve the optical properties of low-temperature chemical grown ZNAs, which will play an important role to prompt its practical application in the future.

In the family of ZnO nanostructures, there are still interesting ones such as nanotubes and quantum dots, which maybe show us much more interesting phenomena in the field of optical properties. Therefore, the extension of this research will be focus on the synthesis, optical properties and maybe devices in the future.

References

[1] M. Fuller, Science 70, 196 (1929).

[2] C. Bunn, Proc. Phys. Soc 47, 835 (1 Sept, 1935).

[3] S. Iijima, Nature 354, 56 (1991).

[4] M. H. Huang, S. Mao, H. Feick, H. G. Yan, Y.Y. Wu, H. Kind, E. Weber, R. Russo, P. D. Yang, Science 292, 1897 (2001).

[5] J. Y. Li, X. L. Chen, H. Li, M. He, Z. Y. Qiao, J. Crys. Growth 233, 5 (2001).

[6] Z. W. Pan, Z. R. Dai, Z. L. Wang, Science 291, 1947 (2001).

[7] J. J. Wu, S. C. Liu, C. T. Wu, K. H. Chen, L. C. Chen, Appl. Phys. Lett. 81, 1312 (2002).

[8] B. D. Yao, Y. F. Chan, N. Wang, Appl. Phys. Lett. 81,757 (2002).

[9] M.J. Zheng, L.D. Zhang, G.H. Li and W. Z. Shen, Chem. Phys. Lett. 363(2002) 123-128

[10] C. H. Liu, J. A. Zapien, Y. Yao, X. M. Meng, C. S. Lee, S. S. Fan, Y. Lifshitz and S. T. Lee, Adv. Mater. 15(2003) 838-841

[11] P. X. Gao and Z. L. Wang, J. Phys. Chem. B, 108 (2004) 7534-7537

[12] J. S. Lee, K. Park, M. I. Kang, I. W. Park, S. W. Kim, W. K. Chom, H. S. Han and S. Kim, J. Cryst. Growth 254 (2003) 423-431.

[13] Q. X. Zhao, P. Klason and M. Willander, Appl. Phys. A, 88 (2007) 27-30.

[14] M. H. Huang, Y. Wu, H. Feick, N. Tran, E .Weber and P. Yang, Adv. Mater. 13 (2001) 113-116.

[15] Y. Sun, G. M. Fuge and M. N. R. Ashfold, Chem. Phys. Lett. 396 (2004) 21-26.

[16] J .Wu and S. C. Liu, Adv .Mater. 14 (2002) 215-218.

[17] W. I. Park, D. H. Kim, S.W. Jung and G. C. Yi, Appl. Phys. Lett. 80 (2002) 4232-4234.

[18] H. D. Yu, Z. P. Zhang, M. Y. Han, X. T. Hao and F. R. Zhu, J. Am. Chem. Soc. 127 (2005) 2378-2379.

[19] L .Vayssieres, K. Keis, S. E. Lindquist and A. Hagfeldt J. Phys. Chem. B 105 (2001) 3350-3352.

[20] L. Vayssieres, Adv. Mater. 15 (2003) 464-466.

[21] Zhong Lin Wang, J. Phys.: Condens. Matter 16 (2004) R829–R858.

[22] O. Dulub, L. A. Boatner and U. Diebold, Surf. Sci. 519 (2002) 201.

[23] B. Meyer and D. Marx, Phys. Rev. B 67 (2003) 035403.

[24] P. W. Tasker, J. Phys. C: Solid State Phys. 12 (1979) 4977.

[25] O. Dulub, U. Diebold and G. Kresse. Phys. Rev. Lett. 90 (2003) 016102.

[26] A. Wander, F. Schedin, P. Steadman, A. Norris, R. McGrath, T. S. Turner, G. Thornton and N.M. Harrison, Phys.Rev. Lett. 86 (2001) 3811.

[27] V. Staemmler, K. Fink, B. Meyer, D. Marx, M. Kunat, S. G. Girol, U. Burghaus and Woll Ch, Phys. Rev. Lett.90 (2003) 106102.

[28] Zinc Oxide bulk, thin films and nanostructures (2006).

[29] T. Kogure, Y. Bando, J. Electron Microsc. 47 (1993) 7903.

[30] A. B. M. A. Ashrafi, A. Ueta, A. Avramescu, H. Kumano, I. Suemune, Y. W. Ok, T. Y. Seong, Appl. Phys. Lett. 76 (2000) 550.

[31] S. K. Kim, S. Y. Seong, C. R. Cho, Appl. Phys. Lett. 82 (2003) 562.

[32] C. H. Bates,W. B. White, R. Roy, Science 137 (1962) 993.

[33] J. E. Jaffe, J. A. Snyder, Z. Lin, A. C. Hess, Phys. Rev. B 62 (2000) 1660.

[34] Y. Li, G.S.Tompa, S. Liang, C. Gorla, C. Lu, J.Doyle, J Vac Sci Techol A 15 (1997) 1663.

[35] D.W. Palmer, Available from: http://www.semiconductors.co.uk, 2002.06.

[36] D, Florescu, L, G, Mourok, F, H, Pollack, D, C, Look, G, Cantwell, X, Li, J Appl Phys., 91(2002)890.

[37] D. Vogel, P. Krüger and J. Pollmann, Phys. Rev. B 52 (1995) R14316.

[38] J. R. Chelikowsky, Solid State Commun. 22 (1977) 351.

[39] U. Rossler, Phys. Rev. 184 (1969) 733.

[40] S. Bloom, I. Ortenburger, Phys. Stat. Sol. (b) 58 (1973) 561.

[41] M. Usuda, N. Hamada, T. Kotani, M. van Schilfgaarde, Phys. Rev. B 66 (2002) 125101.

[42] I. Ivanov, J. Pollmann, Phys. Rev. B 24 (1981) 7275.

[43] D. Vogel, P. Krüger, J. Pollmann, Phys. Rev. B 52 (1995) R14316.

[44] B. K. Meyer, H. Alves, D. M. Hofmann, W. Kriegseis, D. Forster, F. Bertram, J. Christen, A. Hoffmann, M. Straßburg, M. Dworzak, U. Haboeck, A. V. Rodina, Phys. Stat. Sol. (b) 241 (2004) 231.

[45] P. H. Kasai, Phys. Rev. 130, 989 (1963).

[46] K. Vanheusden, W. L. Warren, C. H. Seager, D. R. Tallant, J. A. Voigt, and B. E. Gnade, J. Appl. Phys. 79, 7983 (1996).

[47] S. Yamauchi, Y. Goto, and T. Hariu, J. Cryst. Growth 260, 1 (2004).

[48] M. Liu, A. H. Kitai, and P. Mascher, J. Lumin. 54, 35 (1992).

[49] E. G. Bylander, J. Appl. Phys. 49, 1188 (1978).

[50] X. Yang, G. Du, X. Wang, J. Wang, B. Liu, Y. Zhang, D. Liu, D. Liu,H. C. Ong, and S. Yang, J. Cryst. Growth 252, 275 (2003).

[51] J. Zhong, A. H. Kitai, P. Mascher, and W. Puff, J. Electrochem. Soc. 140, 3644 (1993).

[52] K. Johnston, M. O. Henry, D. M. Cabe, T. Agne, and T. Wichert, Proceedings of the Second Workshop on "SOXESS European Network on ZnO, 27-30 October 2004, Caernarfon, Wales, UK.

[53] R. Dingle, Phys. Rev. Lett. 23, 579 (1969).

[54] Q. X. Zhao, P. Klason, M. Willander, et al., Appl. Phys. Lett. 87, 211912 (2005).

[55] T. Moe Børseth, B. G. Svensson, A. Yu. Kuznetsov, P. Klason, Q. X. Zhao, and M. Willander, Appl. Phys. Lett. 89, 262112 (2006).

[56] P. Klason, T. M. Børseth, Q. X. Zhao, et al., Solid State Communication 145, 321 (2008).

[57] B. K. Meyer, H. Alves, D. M. Hofmann, W. Kriegseis, D. Forster, F. Bertram, J. Christen, A. Hoffmann, M. Straßburg, M. Dworzak, U. Haboeck, and A. V. Rodina, phys. stat. sol. (b) 241(2004) 231– 260.

[58] D. G. Thomas, J. Phys. Chem. Solids 15 (1960) 86.

[59] E. Tomzig and H. Helbig, J. Lumin. 14 (1976) 403.

[60] J. J. Hopfield, J. Phys. Chem. Solids 15 (1960) 97.

[61] D. C. Reynolds, C. W. Litton, and T. C. Collins, Phys. Rev. 140 (1965) A1726.

[62] D. C. Reynolds and T. C. Collins, Phys. Rev. 185 (1969)1099.

[63] E. Fred Schubert, Light-emitting Diodes, second edition, 2006

[64] Z.L. Wang, Materials Today, 7 (2004) 25-33.

[65] R. B. Peterson, C. L. Fields and B. A. Gregg, Langmuir 20 (2004) 5114-5118.

[66] Y. Tak and K. Yong, J. Phys. Chem. B 109 (2005)19263-19269.

[67] C. H. Hung and W. T. Whang, J. Cryst. Growth 268 (2004) 242-248.

[68] X. J. Feng, L. Feng, M. H. Jin, J. Zhai and L. Jiang, J. Am. Chem. Soc. 126 (2004) 62-63.